metals

MDPI

Article

Molecular Docking and Aberration-Corrected STEM of Palladium Nanoparticles on Viral Templates

Liliana Carreño-Fuentes [1,†], Daniel Bahena [2,3], Laura A. Palomares [1], Octavio T. Ramírez [1], Miguel José-Yacamán [3] and Germán Plascencia-Villa [3,4,*]

1 Departamento de Medicina Molecular y Bioprocesos, Instituto de Biotecnología UNAM, Cuernavaca Morelos 62210, Mexico; lilianacarreno@hotmail.com (L.C.-F.); laura@ibt.unam.mx (L.A.P.); tonatiuh@ibt.unam.mx (O.T.R.)

2 CINVESTAV Zacatenco, México City 07360, Mexico; d.bahena.u@gmail.com

3 Department of Physics and Astronomy, Research Centers in Minority Institutions (RCMI), The University of Texas at San Antonio (UTSA), San Antonio, TX 78249, USA; miguel.yacaman@utsa.edu

4 Departamento de Microscopia de Alta Resolución, Universidad Autónoma de San Luis Potosí (UASLP), San Luis Potosí 78210, Mexico

* Correspondence: german.plascenciavilla@utsa.edu; Tel.: +1-210-4587112

† Current Address: Department of Molecular and Cellular Biology, Centro Nacional de Biotecnología/Consejo Superior de Investigaciones Científicas, Madrid 28049, Spain.

Academic Editor: Giuseppe Grasso

Received: 20 June 2016; Accepted: 10 August 2016; Published: 25 August 2016

Abstract: Viral templates are highly versatile biotemplates used for the synthesis of nanostructured materials. Rotavirus VP6 self-assembles into nanotubular hollow structures with well-defined diameters and variable lengths, serving as a nucleic acid-free biotemplate to synthesize metal nanoparticles of controlled size, shape, and orientation. Molecular docking simulations show that exposed residues (H173-S240-D242 and N200-N310) of VP6 have the ability to specifically bind Pd(II) ions, which serve as nucleation sites for the growth and stabilization of palladium nanoclusters. Using VP6 nanotubes as biotemplates allows for obtaining small Pd particles of 1–5 nm in diameter. Advanced electron microscopy imaging and characterization through ultra-high-resolution field-emission scanning electron microscopy (UHR-FE-SEM) and spherical aberration-corrected scanning transmission electron microscopy (Cs-STEM) at a low voltage dose (80 kV) reveals, with high spatial resolution, the structure of Pd nanoparticles attached to the macromolecular biotemplates.

Keywords: proteins; virus; palladium nanoparticles; advanced electron microscopy; molecular docking

1. Introduction

Noble metal nanoparticles and nanoclusters (Au, Ag, Pt, Pd) with sizes below 5 nm are a special type of nanoparticle due to their particular physical, structural, optical, and functional properties [1]. Gold and silver nanoparticles have been widely studied for their fundamental and practical applications, in comparison with a more limited exploration of other transition metal nanoparticles. Palladium nanoparticles have proven potential to be effective catalysts, and important in hydrogen storage, electrochemistry, fuel cells, and sensing [1,2]. To fully exploit the potential of Pd-based nanomaterials, it is necessary to obtain preparations with high control over their size and shape, monodispersion and stability. Different chemical or electrochemical routes have been explored to produce Pd particles, using different stabilizing agents: thiol-based, phosphine ligands, amine-terminated ligands, carbon nanotubes, graphite, polymers (PVP, PVA, PEG), and dendrimers [2–5].

Recently, different biomolecules have shown their utility in nanoscience and nanotechnology, especially to produce water-soluble metal nanoparticles with an exquisite control over their size and shape [6]. A variety of self-assembled biotemplates derived from synthetic peptides, proteins, or viruses have demonstrated their efficiency as adaptable and versatile stabilizing and also structure-directing agents. For this strategy, in the initial reaction step, the metal ion precursors actively bind with correctly located reactive amino acid residues, which may cause partial reduction of precursors forming the nucleation sites. Consequently, upon addition of a reducing agent the additional precursors in the reaction media allow growth of metal nanoparticles over the nucleation sites, obtaining particles directly attached to the biotemplates [6,7]. Viral templates (complete viruses or virus-like particles) stand out as bioscaffolds due to their advantageous inner nanometer-range properties: self-assembly capacity, monodispersity, discrete size and shape, stability, symmetry, and biocompatibility [8]. Palladium nanoparticles were synthesized with Tobacco mosaic virus (TMV) as the scaffold in the aqueous phase [9], as part of hydrogel formulations or through hydrothermal reduction [10–15], producing complete coverage of the viral particles with a Pd layer or the formation of discrete particles of 1–2 nm, depending on reaction conditions. Additionally, genetically engineered M13 bacteriophages were used as biotemplates for Pd particles obtaining hybrid nanorods and nanowires with potential applications in nanobatteries [16,17]. Rotavirus VP6 protein, which composes the middle layer of the viral capsid, has shown versatility as a biotemplate to produce noble metal nanoparticles, including palladium nanoparticles of less than 5 nm in diameter synthesized over the external side of the VP6 nanotubes [18,19], and also the formation of silver nanowires in the interior of the VP6 nanotubes [20]. VP6 assemblies possess an inner capacity for the binding of metal ions (Ca^{2+} and Zn^{2+}), but the specific residues where these interactions take place for functional metals like palladium or platinum are mostly unknown. The study of the interactions of VP6 with metal ions is of high interest, not only for the application of VP6 as biotemplate for nanomaterials, but also due to its clinical relevance as the most antigenic structural protein of rotavirus [21].

Interactions between protein assemblies and metal ions are complex and dynamic due to the large amount of active residues at different reaction conditions. The modeling of the protein-metal complexes generated during the biotemplated synthesis of particles is a key point for understanding and optimizing the reactions occurring. For this purpose, molecular docking simulations, which have been extensively used for drug design and analysis of protein-protein interactions, through different software and algorithms, allow the prediction of the interaction geometries of protein-metal complexes generated and the estimation of the binding affinities. As a result, it is possible to identify metal coordination ligands, coordination chemistry, and positions of metal binding sites [22].

The structure and arrangement of bio-derived metal particles are commonly characterized by transmission electron microscopy (TEM), high-resolution TEM, scanning electron microscopy (SEM), atomic force microscopy (AFM), scanning tunneling microscopy (STM), and also through spectroscopy techniques, such as small angle X-ray scattering (SAXS) and X-ray diffraction (XRD). However, in some cases, when resultant particles are ultra-small, details of their size, shape, structure, and crystallinity are missing due to the technical challenges imposed or simply by the limitation in the resolution of conventional electron microscopy. With the recent development of improved cold field-emission electron guns and the incorporation of spherical aberration correctors into the electron microscope column, nowadays STEM with a high-angle annular dark field detector stands as the instrument of choice for atomic resolution imaging [23]. Among the many advantages of STEM are the ability to directly interpret incoherent Z-contrast (where Z is the atomic number) images, to simultaneously collect EELS or EDX information of the imaged sample, and finally reducing or avoiding radiation damage and ionization of sensitive samples (by the low voltage dose employed) while keeping atomic resolution.

In this work, we report the study of palladium nanoparticles directly attached to recombinantly produced VP6 tubular assemblies, producing an integrative hybrid nanomaterial with high control over the Pd particle size and arrangement over the biotemplates. Molecular docking simulations

of Pd(II) precursors and VP6 protein structure helped to specifically determine the metal binding sites located over the external layer of protein nanotubes, which served as initial nucleation sites during the synthesis and posterior stabilization of Pd nanoparticles. Aberration-corrected scanning transmission electron microscopy (Cs-STEM) allowed obtaining atomic-resolution imaging of the small Pd nanoparticles of 1–5 nm in diameter, determining their structure, crystallinity, and arrangement with high spatial sub-angstrom resolution. Remarkably, Cs-STEM was able to image single Pd atoms attached to the protein templates, which eventually may grow to form the nanoparticles, confirming the high affinity of VP6 for Pd.

2. Experimental Section

2.1. Recombinant Production of Viral Templates

Rotavirus VP6 nanotubes were produced using the insect-cell baculovirus expression vector system, by infecting HighFive cells (*Trichoplusia ni*) with bacVP6 at multiplicity of infection (MOI) of 0.1 and harvesting cell culture media supernatant at 96 hpi (hours post-infection). Self-assembled nanotubes were purified by continuous steps of ultrafiltration (Amicon, 30000 NMWL, EMD Millipore, Darmstadt, Germany), ion exchange chromatography (Q-Sepharose, Amersham, GE Healthcare Bio-Sciences, Pittsburgh PA, USA), and size-exclusion chromatography (HW65F, TOSOH Bioscience, Grove City, OH, USA) [18].

2.2. Molecular Docking Simulations

Molecular modeling of VP6 trimer and VP6 hexamers was performed with USCF Chimera v1.10 (UCSF, San Francisco, CA, USA) and PyMOL V1.5 (Schrödinger, Cambridge MA, USA), based on PDB: 1QHD, 3N09, and 3IYU [24–26]. Structures were optimized in the YASARA server [27], and protonation states at pH 5 or 8 were calculated by the PDB2PQR web server [28]. Metal binding sites and binding energy were predicted with AutoDock 4.0 package (The Scripps Research Institute, La Jolla, CA, USA) [29,30], with similar parameter conditions optimized previously [20].

2.3. In Situ Synthesis of Pd Nanoparticles

Purified VP6 nanotubes were concentrated with tangential flow filtration system (Millipore, Centricon 100 kDa, EMD Millipore, Darmstadt, Germany) to perform buffer exchange from Tris-EDTA (30 mM, 0.1 mM, pH 8.0) to ddH_2O, quantified by Bradford assay and diluted to achieve 25 $\mu g \cdot mL^{-1}$ of pure protein nanotubes. Palladium nanoparticles were produced in situ by adding to the protein solution K_2PdCl_4 (Sigma-Aldrich, St. Louis, MO, USA) aqueous solution to achieve 0.5 mM final concentration. Samples were mixed gently by inversion and incubated for 3 h at room temperature; finally $NaBH_4$ (Sigma-Aldrich) was added to a final concentration of 1 mM and incubated for an additional hour. VP6-Pd nanotubes were allowed to precipitate, the supernatant removed and suspended in pure ddH_2O for further analysis.

2.4. Advanced Electron Microscopy Imaging

VP6 nanotubes with Pd particles were characterized by ultra-high-resolution field-emission scanning electron microscopy (UHR FE-SEM, HITACHI HighTech S-5500, Schaumburg, IL, USA) of samples mounted on ultra-flat silicon wafer chips (Ted Pella, Redding, CA, USA). Cs-STEM imaging with BF and HAADF detectors (Atomic Resolution Analytical Microscope JEM-ARM200F (JEOL, Peabody, MA, USA), with CEOS spherical aberration corrector and operated at accelerating voltage of 80 kV), coupled with energy dispersive X-ray spectroscopy (EDAX, Mahwah, NJ, USA) was performed with samples deposited over carbon/formvar 300 mesh copper grids (Electron Microscopy Sciences, Hatfield, PA, USA). Micrographs were recorded and analyzed with DigitalMicrograph (GATAN, Pleasanton, CA, USA).

3. Results and Discussion

Molecular Binding Simulation VP6-Pd(II)

In this work, we implemented molecular simulations to gain a deeper understanding of the initial steps occurring during the bio-directed synthesis of Pd nanoparticles. Particularly, to identify the amino acid residues implicated in the active binding of Pd(II) ions at the specific reaction conditions established. Docking simulations were performed between crystalline structure of VP6 (1QHD) [25], assembled as trimmers, and two different ionic species of Pd(II). When K_2PdCl_4 is dissolved in aqueous solution a mixture of complexes is formed. This Pd(II) speciation is dependent on Cl^- concentration [31,32]. In our case, since the K_2PdCl_4 was used immediately after dissolution in ddH_2O and no additional Cl^- ions were added, the negatively charged species of Pd(II), like $PdCl_3(OH)^-$ and $PdCl_4^{2-}$ were the most abundant species [31], and chosen for the molecular docking. The protonation state of VP6 was also taken into consideration as a critical parameter for the in silico interactions with Pd anions. Table 1 contains the identified VP6 residues and their calculated binding energies by molecular docking not previously reported, that effectively interact with Pd species in aqueous media.

Table 1. Molecular docking VP6 trimer with Pd(II) ions. Datasets obtained from the molecular docking of VP6 trimer with $PdCl_3(H_2O)^-$ or $PdCl_4^-$ at pH 5 or 8 using AutoDock 4.0 software (The Scripps Research Institute, La Jolla, CA, USA). Residues and binding energies determined for each simulation performed.

pH of Simulation	$PdCl_3(H_2O)^-$		$PdCl_4^-$	
	Residues	**Binding Energy (ΔG)**	**Residues**	**Binding Energy (ΔG)**
5.0	His173 Ser240 Asp242	-2.0 kcal·mol^{-1}	Ser169 Gln170 His173	-0.80 kcal·mol^{-1}
8.0	Asn200 Asn310	-1.2 kcal·mol^{-1}	Pro309 Asn310 Ala311	-0.15 kcal·mol^{-1}

The metal binding sites for Pd(II) of VP6 identified here by molecular docking were situated at the top of the trimer structure. These sites were in the side region facing between trimers and close to the pore formed by the hexagonal array of VP6 trimers (Figure 1A). From the two Pd species, $PdCl_3(H_2O)^-$ showed the higher binding energy with -2.0 and -1.2 kcal·mol^{-1} at pH of 5.0 and 8.0, respectively. Previous reports have proved that the major species of Pd in solution under similar physicochemical conditions is $PdCl_3(H_2O)^-$ [4,5] which, in our case, was attributed as the ion responsible for nucleation of particles. Molecular docking showed that Pd(II) species interacted with charged and polar residues of VP6, such as Asp, His, Ser, Gln, and Asn. The metal binding site formed by a His173, Ser240 and Asp242 which, by their location and 3D arrangement, had distances of 3.8, 4.2, and 5.5 Å (Figure 1B). This allowed the stabilization of the Pd(II) precursor by the formation of hydrogen bonds (predicted by the simulations) between Pd ions with protonated side chains from Ser and Asp residues, nitrogen from imidazole (His173), and not only by the electrostatic attraction of metal ions and residues [32–34].

The second favorable binding site formed by Asn200 and Asn310, also located on the external side of the nanotubes, was predicted to interact with Pd(II) through a weak hydrogen bond (total ΔG = -1.2 kcal·mol^{-1}) (Figure 1C). The amino acids forming the Pd binding sites are electrostatically charged or polar residues. All of them have demonstrated high affinity for Pd, especially His [35]. Similar to the observations here, His, Asn, and Arg residues of synthetic peptides effectively served as nucleation and stabilizing agents to obtain Pd nanoparticles [36].

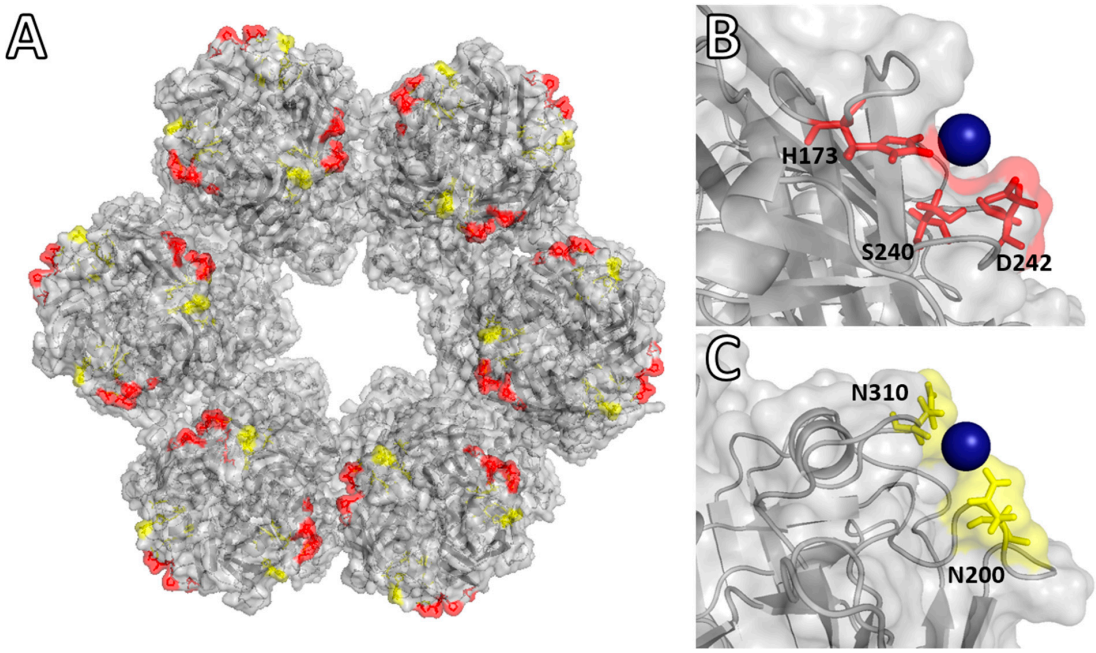

Figure 1. Molecular docking VP6 trimer with Pd(II) ions. (**A**) Hexamer of six trimers of VP6, indicating binding sites for $PdCl_3(H_2O)^-$ at pH 5.0 (red) and pH 8.0 (yellow). (**B**) Pd(II) binding site at pH 5.0. (**C**) Pd(II) binding site at pH 8.0. Molecular modeling with UCSF Chimera v1.10 and PyMOL V1.5 (Schröndinger) with PDB files 1QHD, 3N09, and 3IYU [24–26].

Several reports have shown the need for site-directed mutations to insert Cys residues in TMV, providing active sites for the adsorption and reduction of Pd(II) ions and other metal precursors [9,15]. However, wild-type TMV has also proved to be able to stabilize these precursor ions, suggesting that other amino acid residues are involved [9]. In the case of VP6, the domains exposed to the external face of nanotubes do not have Cys residues that may act as metal binding sites, supporting the hypothesis that intrinsic metal affinity could be potentiated or custom modified by site-directed mutagenesis at protein domains predicted in this work by molecular docking.

Figure 2 shows UHR FE-SEM imaging of VP6 nanotubes functionalized with Pd. Low magnification FE-SEM allowed us to have a general view to confirm the formation and location of high-contrast Pd nanoparticles. Samples were directly mounted on ultra-flat silicon wafers, without the addition of any contrast agent (neither heavy-metal negative staining, nor plasma coating). The contrast was generated only by the scattering of secondary electrons caused by the metallic Pd nanoparticles directly attached to the protein templates. High magnification FE-SEM imaging confirmed that the diameter and arrangement of protein templates supported the initial formation of VP6-Pd(II) nucleation sites during the first 1 h of reaction and the final formation of nanoparticles upon the addition of reductant ($NaBH_4$) without perceivable disassembly of VP6 nanotubes. VP6 self-assembles into tubes with a diameter of 75 nm in the pH range of 5.5–7.0, and may support divalent cations up to 200 mM, keeping its macrostructural arrangement [37].

Cs-STEM imaging at low magnification provided a general view of the protein nanotubes conjugated with Pd (Figure 3). The size distribution of Pd ranged from 1–5 nm, with a media of 2.5 ± 1.02 nm in diameter (Figure S1). EDX spectroscopy confirmed the presence of palladium, with a prominent presence of characteristic X-ray peak of Pd centered at 2.838 keV (Figure 3C). The rest of the peaks corresponded to copper and aluminum (from the grid and holder, respectively), and light elements (C, N, O) from the protein template and carbon support. The results of nanoparticle sizes achieved in this work are in accordance with previous reports where it was demonstrated that $PdCl_3(H_2O)^-$ ionic species promotes the formation of small Pd nanoparticles [4,5], which reinforce the observations from the molecular simulation experiments.

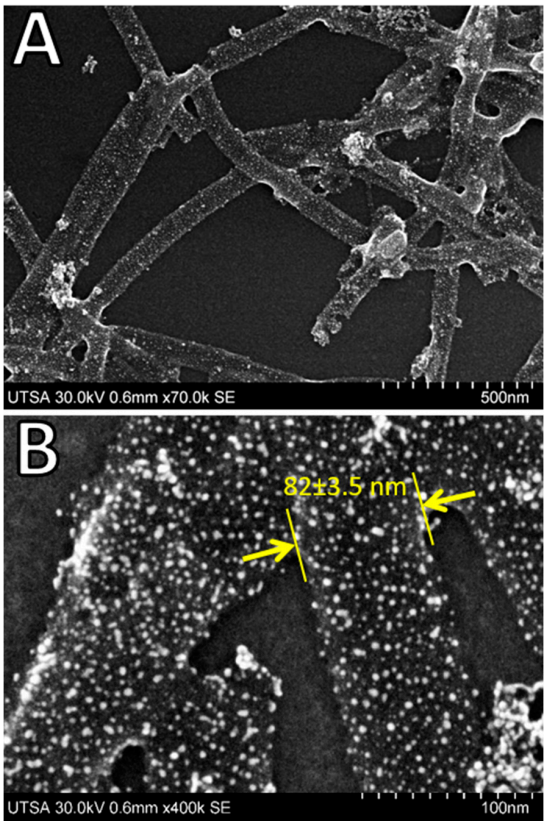

Figure 2. FE-SEM imaging of VP6-Pd. (**A**) Low magnification SEM. (**B**) High magnification SEM, indicating nanotube diameter of 82 ± 3.5 nm. Imaging with UHR-FE-SEM HITACHI, operated at an accelerating voltage of 30 kV.

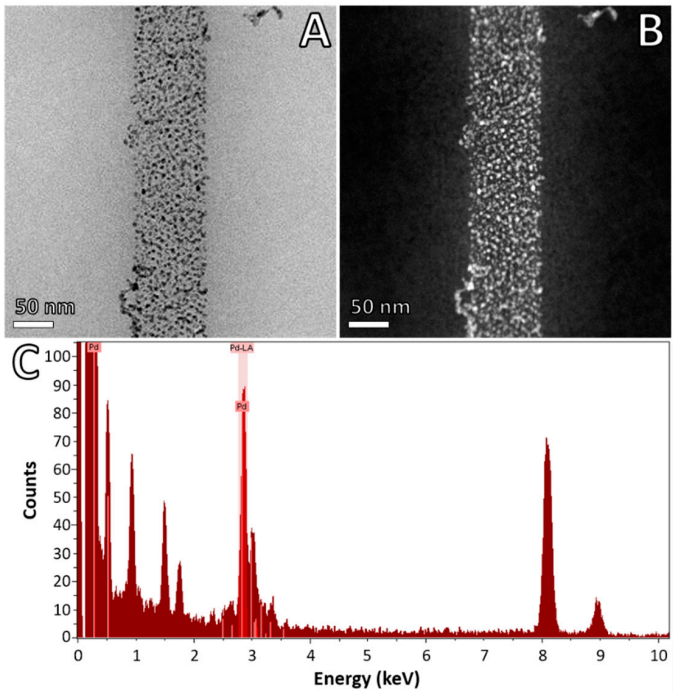

Figure 3. Atomic resolution Cs-STEM imaging. (**A**) BF-STEM imaging. (**B**) HAADF-STEM imaging. (**C**) EDX spectra. Imaging with JEM ARM-200F (JEOL), operated at accelerating voltage of 80 kV in STEM mode.

Comparing previous reports of rotavirus VP6, TMC-cys, M13, and synthetic peptides as bio-templates for the synthesis of Pd nanoparticles, the diameter of the particles, structure, crystallinity, and catalytic activity of the particles can be tuned depending of the Pd precursor, concentration, and reducing agent, and in some cases by the reaction temperature [9,14,16,19,38,39]. Our results of molecular docking also demonstrated that the high affinity residues on VP6 helped to constrain the size and distribution of Pd particles all over the bio-template external surface. In particular, it has been demonstrated that the presence of His residues is critical within model synthetic peptides, to bio-direct the formation of ~2 nm Pd nanoparticles, while their substitution by Ala produce particles with a higher diameter (~4 nm) [36].

In contrast, colloidal synthesis of Pd using 1-dodecanethiol as a surfactant produced particles with bimodal distribution: one population with ~5 nm and another corresponding to small clusters with 1–2 nm in diameter [40]. Absorbance spectroscopy of VP6-Pd (Figure S2) did not show any prominent absorption peaks, contrary to the very well-defined peaks in Ag and Au, correlating with observation of small diameters of particles and indication of complete reduction of Pd precursors.

High-resolution Cs-STEM imaging of VP6-derived Pd particles is shown in Figure 4. A HAADF detector provided high contrast for electrodense Pd aggregates in comparison with the bright field (BF) detector (Figure 4A,B). Most of the Pd was located in well-defined nanoparticulate aggregates, but, remarkably, HAADF-STEM revealed the presence of high contrast individual Pd atoms attached to the protein surface (Figure 4B and Figure S3) not previously observed on virus-derived hybrid nanomaterials characterized with conventional TEM. The advantage of HAADF detector is allowing a direct interpretation of incoherent Z-contrast (where Z is atomic number), in this case to easily distinguish Pd atoms from low contrast light atoms forming the proteins. Importantly, new generation STEM instruments accessorized with a spherical aberration corrector can reach sub-angstrom resolution (<0.70 Å) even at low accelerating voltages (60–80 keV) [23]. This spatial resolution was previously only possible at high voltages of 300 keV, but with the risk of irreversibly damaging or altering the sample integrity due to the high electron dose needed. Cs-STEM imaging of Pd nanoparticles clearly revealed the crystallinity of the small particles and the atomistic structure. The Pd particle shown in Figure 4C corresponded with an fcc (face centered cubic) structure with a well-defined hexagonal shape [40]. The FFT pattern indicated that it was oriented in (011) with respect to the electron beam structure. Atomic resolution HAADF-STEM imaging revealed, in detail, the interplanar distances of 2.57 and 2.49 Å (Figure 4D), whereas the intensity profile over the nanoparticle surface clearly showed the regular stepped arrangement of palladium columns with a regular spacing of 0.249 nm (Figure 4E).

The fcc cubo-octahedral structure of Pd is a highly stable arrangement adopted preferentially by noble metals in nanometer-scale particles. Other structures found in palladium include single twinned, icosahedral, and decahedral configurations, but in most of the cases it is strictly necessary to add surfactants and coating agents to direct and stabilize the final structure. The coating or structure-stabilizing agents directly influence the atomic arrangement and stability of small Pd particles; particularly, the amine-protected Pd nanoparticles result in well-defined and more stable structures compared to the thiol-protected particles [3,41]. Our results correlated with the formation of well-defined stable configurations and crystalline fcc Pd particles. Figure 5 shows another fcc Pd particle, but with (001) orientation. Similarly, BF/HAADF-STEM clearly showed the atomic structure reached on the virus-derived particle. The FFT pattern and high magnification of the Pd nanoparticle showed the square distribution contrast of the surface, with high regular arrangement forming a crystalline structure. Measurement of the lattice spacing showed a value of 2.15 Å and the angles between planes showed no perceivable distortions. Energy-dispersive X-ray spectroscopy (EDX) allowed us to visually map and to confirm that the particles effectively corresponded to Pd. Figure S4 shows that high-contrast nanoparticles observed though HAADF-STEM detector co-localized with X-ray spectrum mapping image of Pd-L series signal (2.984 keV, areas shown in red). Integration and deconvolution of characteristic peaks indicated that virus-derived hybrid nanomaterials contained 56.3% ± 7.3% of Pd (normalized weight) or 12.8% ± 1.6% of atoms, the remaining 43.7% ± 3.2% weight

(87.6% ± 6.3% atoms) assigned to light elements (C, N, O) from the protein biotemplate and carbon support. Palladium nanoparticles with such size obtained though virus-templated synthesis have potential uses in hydrogen storage, electrochemistry, fuel cells and sensing applications. Pd particles have emerged as versatile, convenient and selective catalyst [42], especially small nanoparticles (<5 nm) with highly reactive surfaces, with wide acceptability in organic synthesis, coupling reactions, and heterogeneous catalysis.

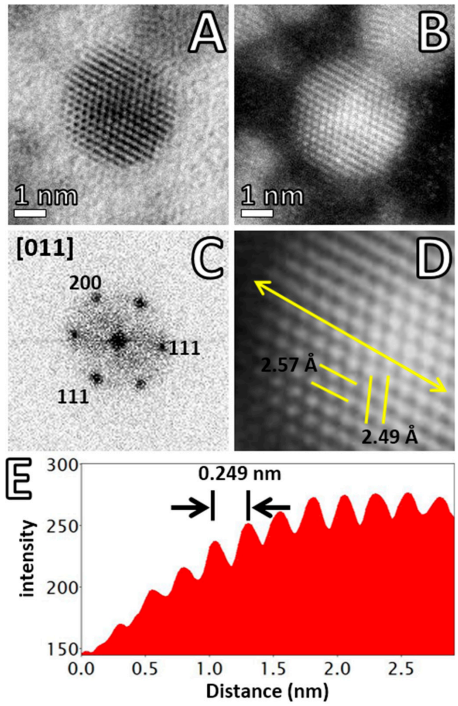

Figure 4. Atomic resolution Cs-STEM imaging. (**A**) BF-STEM imaging. (**B**) HAADF-STEM imaging. (**C**) FFT pattern. (**D**) Detail of palladium nanoparticle with interplanar distances. (**E**) Intensity profile of arrow in (**D**). Imaging with JEM ARM-200F (JEOL), operated at an accelerating voltage of 80 kV in STEM mode.

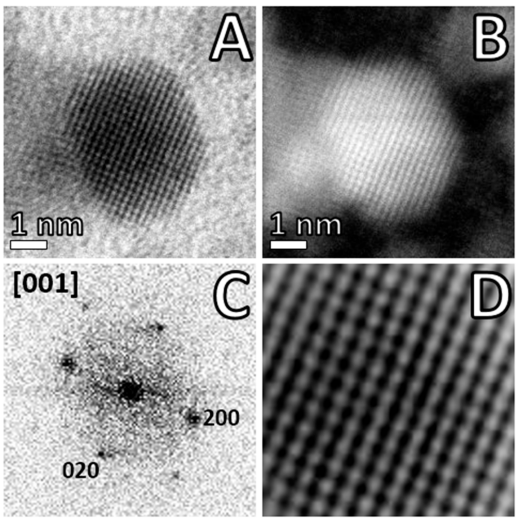

Figure 5. Atomic resolution Cs-STEM imaging. (**A**) BF-STEM imaging. (**B**) HAADF-STEM imaging. (**C**) FFT pattern. (**D**) Detail of palladium nanoparticle with crystalline arrangement. Imaging with JEM ARM-200F (JEOL), operated at an accelerating voltage of 80 kV in STEM mode.

4. Conclusions

Molecular docking simulations and integrative advanced electron microscopy imaging showed that self-assembled macromolecular templates derived from rotavirus proteins provided a platform to patterning functional materials at the molecular and even atomic scale. The use of rotavirus VP6 nanotubes to effectively control nucleation, growth, and spatial location of palladium precursors allowed generating highly-ordered hybrid nanostructures with advanced functionality for nanotechnological applications. VP6 nanotubes kept their symmetry and three-dimensional arrangement upon functionalization with Pd, indicating the high stability and ordering by extensive electrostatic interactions between trimeric subunits. Molecular docking provided important information on the precise location of metal binding sites (His173-Ser240-Asp242 and Asn200-Asn310) for $PdCl_3(H_2O)^-$ over the protein biotemplates, which eventually can be used for control and optimization of reaction conditions, as well as the custom design of high-order protein assemblies with novel functionalities. Advanced nanomaterials require the use of advanced imaging techniques; in particular, spherical aberration-corrected STEM and ultra-high-resolution SEM allowed revealing, in high detail, the arrangement adopted by Pd over the protein biotemplates. Interestingly, in addition to highly-stable 1–5 nm fcc particles, it was possible to directly image single Pd atoms attached over the protein surfaces, confirming high affinity of VP6 for Pd species.

Supplementary Materials: The following are available online at http://www.mdpi.com/2075-4701/6/9/200/s1. Absorbance spectra, histogram size distribution Pd particles, Atomic resolution Cs-STEM imaging and EDX mapping.

Acknowledgments: This work was supported by The Welch Foundation (AX-1615), PAPIIT-UNAM (IT 200416), and NIH Research Centers in Minority Institutions (RCMI) Program: NIH RCMI Nanotechnology and Human Health Core (#5G12RR013646-12) and NIH RCMI Biophotonics Core (#G12MD007591). Facilities of Kleberg Advanced Microscopy Center (KAMiC) at UTSA. L.C.-F. was supported by a CONACYT fellowship.

Author Contributions: L.C.-F. L.A.-P., O.T.-R. and G.P.-V. conceived and designed the experiments; L.C.-F. performed the experiments; D.B, M.J.-Y. and G.P.-V. performed imaging, L.C.-F., D.B. and G.P.-V. analyzed the data; O.T.R., L.A.P and M.J.-Y. contributed reagents/materials/analysis tools; L.C.-F. and G.P.-V. wrote the paper.

Conflicts of Interest: The authors declare no conflict of interest.

References

1. Yuan, X.; Dou, X.; Zheng, K.; Xie, J. Recent advances in the synthesis and applications of ultrasmall bimetallic nanoclusters. *Part. Part. Syst. Charact.* **2015**, *32*, 613–629.
2. James, C. The preparation of palladium nanoparticles. *Platin. Met. Rev.* **2012**, *56*, 83–98.
3. Corthey, G.; Rubert, A.A.; Picone, A.L.; Casillas, G.; Giovanetti, L.J.; Ramallo-López, J.M.; Zelaya, E.; Benitez, G.A.; Requejo, F.G.; José-Yacamán, M.; et al. New insights into the chemistry of thiolate-protected palladium nanoparticles. *J. Phys. Chem. C* **2012**, *116*, 9830–9837.
4. Kettemann, F.; Wuithschick, M.; Caputo, G.; Kraehnert, R.; Pinna, N.; Rademann, K.; Polte, J. Reliable palladium nanoparticle syntheses in aqueous solution: The importance of understanding precursor chemistry and growth mechanism. *CrystEngComm* **2015**, *17*, 1865–1870.
5. Scott, R.W.J.; Ye, H.; Henriquez, R.R.; Crooks, R.M. Synthesis, characterization, and stability of dendrimer-encapsulated palladium nanoparticles. *Chem. Mater.* **2003**, *15*, 3873–3878.
6. Dickerson, M.B.; Sandhage, K.H.; Naik, R.R. Protein- and peptide-directed syntheses of inorganic materials. *Chem. Rev.* **2008**, *108*, 4935–4978.
7. Slocik, J.M.; Wright, D.W. Biomimetic mineralization of noble metal nanoclusters. *Biomacromolecules* **2003**, *4*, 1135–1141.
8. Strable, E.; Finn, M.G. Chemical modification of viruses and virus-like particles. *Curr. Top. Microbiol. Immunol.* **2009**, *327*, 1–21.
9. Lim, J.S.; Kim, S.M.; Lee, S.Y.; Stach, E.A.; Culver, J.N.; Harris, M.T. Quantitative study of Au(III) and Pd(II) ion biosorption on genetically engineered Tobacco mosaic virus. *J. Colloid Interface Sci.* **2010**, *342*, 455–461.
10. Lewis, C.L.; Lin, Y.; Yang, C.; Manocchi, A.K.; Yuet, K.P.; Doyle, P.S.; Yi, H. Microfluidic fabrication of hydrogel microparticles containing functionalized viral nanotemplates. *Langmuir* **2010**, *26*, 13436–13441.

11. Manocchi, A.K.; Horelik, N.E.; Lee, B.; Yi, H. Simple, readily controllable palladium nanoparticle formation on surface-assembled viral nanotemplates. *Langmuir* **2010**, *26*, 3670–3677.
12. Manocchi, A.K.; Seifert, S.; Lee, B.; Yi, H. On the thermal stability of surface-assembled viral-metal nanoparticle complexes. *Langmuir* **2010**, *26*, 7516–7522. [PubMed]
13. Manocchi, A.K.; Seifert, S.; Lee, B.; Yi, H. In situ small-angle X-ray scattering analysis of palladium nanoparticle growth on tobacco mosaic virus nanotemplates. *Langmuir* **2011**, *27*, 7052–7058.
14. Yang, C.; Choi, C.H.; Lee, C.S.; Yi, H. A facile synthesis-fabrication strategy for integration of catalytically active viral-palladium nanostructures into polymeric hydrogel microparticles via replica molding. *ACS Nano* **2013**, *7*, 5032–5044.
15. Adigun, O.O.; Freer, A.S.; Miller, J.T.; Loesch-Fries, L.S.; Kim, B.S.; Harris, M.T. Mechanistic study of the hydrothermal reduction of palladium on the Tobacco mosaic virus. *J. Colloid Interface Sci.* **2015**, *450*, 1–6.
16. Oh, D.; Qi, J.; Lu, Y.C.; Zhang, Y.; Shao-Horn, Y.; Belcher, A.M. Biologically enhanced cathode design for improved capacity and cycle life for lithium-oxygen batteries. *Nat. Commun.* **2013**, *4*, 2756.
17. Zhou, J.C.; Soto, C.M.; Chen, M.S.; Bruckman, M.A.; Moore, M.H.; Barry, E.; Ratna, B.R.; Pehrsson, P.E.; Spies, B.R.; Confer, T.S. Biotemplating rod-like viruses for the synthesis of copper nanorods and nanowires. *J. Nanobiotechnol.* **2012**, *10*, 18.
18. Plascencia-Villa, G.; Mena, J.A.; Castro-Acosta, R.M.; Fabian, J.C.; Ramirez, O.T.; Palomares, L.A. Strategies for the purification and characterization of protein scaffolds for the production of hybrid nanobiomaterials. *J. Chromatogr. B* **2011**, *879*, 1105–1111.
19. Plascencia-Villa, G.; Saniger, J.M.; Ascencio, J.A.; Palomares, L.A.; Ramirez, O.T. Use of recombinant rotavirus VP6 nanotubes as a multifunctional template for the synthesis of nanobiomaterials functionalized with metals. *Biotechnol. Bioeng.* **2009**, *104*, 871–881. [CrossRef] [PubMed]
20. Carreno-Fuentes, L.; Ascencio, J.A.; Medina, A.; Aguila, S.; Palomares, L.A.; Ramirez, O.T. Strategies for specifically directing metal functionalization of protein nanotubes: Constructing protein coated silver nanowires. *Nanotechnology* **2013**, *24*, 235602. [CrossRef] [PubMed]
21. Pastor, A.R.; Rodriguez-Limas, W.A.; Contreras, M.A.; Esquivel, E.; Esquivel-Guadarrama, F.; Ramirez, O.T.; Palomares, L.A. The assembly conformation of rotavirus VP6 determines its protective efficacy against rotavirus challenge in mice. *Vaccine* **2014**, *32*, 2874–2877. [CrossRef] [PubMed]
22. Seebeck, B.; Reulecke, I.; Kamper, A.; Rarey, M. Modeling of metal interaction geometries for protein-ligand docking. *Proteins* **2008**, *71*, 1237–1254. [CrossRef] [PubMed]
23. Pennycook, S.J. Scanning transmission electron microscopy: Seeing the atoms more clearly. *MRS Bull.* **2012**, *37*, 943–951. [CrossRef]
24. Chen, J.Z.; Settembre, E.C.; Aoki, S.T.; Zhang, X.; Bellamy, A.R.; Dormitzer, P.R.; Harrison, S.C.; Grigorieff, N. Molecular interactions in rotavirus assembly and uncoating seen by high-resolution cryo-EM. *Proc. Natl. Acad. Sci. USA* **2009**, *106*, 10644–10648. [CrossRef] [PubMed]
25. Mathieu, M.; Petitpas, I.; Navaza, J.; Lepault, J.; Kohli, E.; Pothier, P.; Prasad, B.V.; Cohen, J.; Rey, F.A. Atomic structure of the major capsid protein of rotavirus: Implications for the architecture of the virion. *EMBO J.* **2001**, *20*, 1485–1497. [CrossRef] [PubMed]
26. Zhang, X.; Settembre, E.; Xu, C.; Dormitzer, P.R.; Bellamy, R.; Harrison, S.C.; Grigorieff, N. Near-atomic resolution using electron cryomicroscopy and single-particle reconstruction. *Proc. Natl. Acad. Sci. USA* **2008**, *105*, 1867–1872. [CrossRef] [PubMed]
27. Krieger, E.; Joo, K.; Lee, J.; Raman, S.; Thompson, J.; Tyka, M.; Baker, D.; Karplus, K. Improving physical realism, stereochemistry, and side-chain accuracy in homology modeling: Four approaches that performed well in CASP8. *Proteins* **2009**, *77*, 114–122. [CrossRef] [PubMed]
28. Dolinsky, T.J.; Czodrowski, P.; Li, H.; Nielsen, J.E.; Jensen, J.H.; Klebe, G.; Baker, N.A. PDB2PQR: Expanding and upgrading automated preparation of biomolecular structures for molecular simulations. *Nucleic Acids Res.* **2007**, *35*, W522–W525. [CrossRef] [PubMed]
29. Huey, R.; Morris, G.M.; Olson, A.J.; Goodsell, D.S. A semiempirical free energy force field with charge-based desolvation. *J. Comput. Chem.* **2007**, *28*, 1145–1152. [CrossRef] [PubMed]
30. Morris, G.M.; Goodsell, D.S.; Halliday, R.S.; Huey, R.; Hart, W.E.; Belew, R.K.; Olson, A.J. Automated docking using a Lamarckian genetic algorithm and an empirical binding free energy function. *J. Comput. Chem.* **1998**, *19*, 1639–1662. [CrossRef]

31. Talanova, G.G.; Yatsimirskii, K.B.; Kravchenko, O.V. Peculiarities of K_2PdCl_4 and K_2PtCl_4 Complexation with Polymer-Supported Dibenzo-18-crown-6. *Ind. Eng. Chem. Res.* **2000**, *39*, 3611–3615. [CrossRef]
32. Li, J.H.; Byrne, R.H. Amino acid complexation of palladium in seawater. *Environ. Sci. Technol.* **1990**, *24*, 1038–1041. [CrossRef]
33. Odani, A.; Yamauchi, O. Ternary α-amino acid-palladium(II) complexes with ligand-ligand hydrogen bonding. *Bull. Chem. Soc. Jpn.* **1981**, *54*, 3773–3779. [CrossRef]
34. Wilson, E.W.; Martin, R.B. Circular dichroism of palladium(II) complexes of amino acids and peptides. *Inorg. Chem.* **1970**, *9*, 528–532. [CrossRef]
35. Sugahara, M.; Asada, Y.; Shimada, H.; Taka, H.; Kunishima, N. HATODAS II—Heavy-atom database system with potentiality scoring. *J. Appl. Crystallogr.* **2009**, *42*, 540–544.
36. Coppage, R.; Slocik, J.M.; Sethi, M.; Pacardo, D.B.; Naik, R.R.; Knecht, M.R. Elucidation of peptide effects that control the activity of nanoparticles. *Angew. Chem.* **2010**, *49*, 3767–3770. [CrossRef] [PubMed]
37. Lepault, J.; Petitpas, I.; Erk, I.; Navaza, J.; Bigot, D.; Dona, M.; Vachette, P.; Cohen, J.; Rey, F.A. Structural polymorphism of the major capsid protein of rotavirus. *EMBO J.* **2001**, *20*, 1498–1507. [CrossRef] [PubMed]
38. Bedford, N.M.; Ramezani-Dakhel, H.; Slocik, J.M.; Briggs, B.D.; Ren, Y.; Frenkel, A.I.; Petkov, V.; Heinz, H.; Naik, R.R.; Knecht, M.R. Elucidation of peptide-directed palladium surface structure for biologically tunable nanocatalysts. *ACS Nano* **2015**, *9*, 5082–5092. [CrossRef] [PubMed]
39. Bhandari, R.; Knecht, M.R. Isolation of template effects that control the structure and function of nonspherical, biotemplated Pd nanomaterials. *Langmuir* **2012**, *28*, 8110–8119. [CrossRef] [PubMed]
40. José-Yacamán, M.; Marín-Almazo, M.; Ascencio, J.A. High resolution TEM studies on palladium nanoparticles. *J. Mol. Catal. A Chem.* **2001**, *173*, 61–74. [CrossRef]
41. Corthey, G.; Olmos-Asar, J.A.; Casillas, G.; Mariscal, M.M.; Mejía-Rosales, S.; Azcárate, J.C.; Larios, E.; José-Yacamán, M.; Salvarezza, R.C.; Fonticelli, M.H. Influence of capping on the atomistic arrangement in palladium nanoparticles at room temperature. *J. Phys. Chem. C* **2014**, *118*, 24641–24647. [CrossRef]
42. Bej, A.; Ghosh, K.; Sarkar, A.; Knight, D.W. Palladium nanoparticles in the catalysis of coupling reactions. *RSC Adv.* **2016**, *6*, 11446–11453. [CrossRef]